Universität des Saarlandes

Fachrichtung 6.1 – Mathematik

Preprint Nr. 212

Retinal vessel detection via second derivative of local Radon transform

Michael Krause, Ralph M. Alles,
Bernhard Burgeth and Joachim Weickert

Saarbrücken 2008

Fachrichtung 6.1 – Mathematik
Universität des Saarlandes

Preprint No. 212
submitted: 27.06.2008, update: 01.10.2009

Retinal vessel detection via second derivative of local Radon transform

Michael Krause
University of Bayreuth
Ceramic Materials Engineering
95440 Bayreuth
Germany
michael.krause@uni-bayreuth.de

Ralph M. Alles
Zeughausstr. 7b
66740 Saarlouis
Germany
email2005@dr-alles.de

Bernhard Burgeth
Saarland University
Department of Mathematics and Computer Science
66041 Saarbrücken
Germany
burgeth@math.uni-sb.de

Joachim Weickert
Saarland University
Department of Mathematics and Computer Science
66041 Saarbrücken
Germany
weickert@mia.uni-saarland.de

Edited by
FR 6.1 – Mathematik
Universität des Saarlandes
Postfach 15 11 50
66041 Saarbrücken
Germany

Fax: + 49 681 302 4443
e-Mail: preprint@math.uni-sb.de
WWW: http://www.math.uni-sb.de/

Abstract

For the automatic detection of retinal blood vessels a preprocessing of the noisy original images is necessary. Retinal blood vessels are assumed to be line-like structures and can therefore be enhanced via convolution with suitable, elongated kernels. Consequently we use the local Radon kernel as a prototype of an elongated kernel for this task. The Radon kernel is rotated at different angles and adapts via a maximisation procedure to the directions of the vessels. The proposed algorithm is easy to implement and combined with edge- and coherence-enhancing anisotropic diffusion as a preprocessing step it offers higher robustness than the Laplacian of Gaussian or Haralick operator. Furthermore, our algorithm detects vessels as connected structures with very few interruptions. The performance is evaluated in experiments on the publicly available databases DRIVE and STARE as well as on selected examples of our clinical database. Since our algorithm does not depend on a priori directional and branching models, in its generality it is capable to detect other vessel structures in the human eye such as the conjunctiva vessels.

Keywords: Retinal imaging, vessel detection, vessel segmentation, local Radon transform, conjunctiva vessels

1 Introduction

The inspection of the retinal vessels is a well established and scientifically evaluated method for the screening of important vascular diseases. The increasing availability of so called "Non-Mydriatic" cameras will make digital imaging a very important part of the ophthalmologists work. Ophthalmologists can now create considerable statistical databases which prepare the path for unprecedented numerical and statistical analysis. Similar to cardiac or brain vascular investigation, retinal vessel analysis is an "in vivo" method. This paper derives a novel approach for relatively simple and effective retinal vessel detection and segmentation, inspired by mathematical models of computerised tomography (Natterer, 1986), especially Rieder et al. (2000) and Krause (2006).

1.1 Related work

Retinal vessel segmentation algorithms can be grouped into various categories. Some algorithms use tracking methods to detect vessels (Cree et al., 2005), Gao et al. (1997), Niemeijer et al. (2007), starting from an initial

point, which can be chosen for example near the optic nerve (Jelinek et al., 2005). Other methods as described in Chapman et al. (2001), Lowell et al. (2004), Hoover et al. (2000), Chanwimaluang and Fan (2003), M.Sofka and Stewart (2006), Gang et al. (2002) rely on matched filter response techniques: A shape model that resembles the vessel cross-section is convolved with the image and rotated by several angles in the search for an optimal fit. The filter exists in one or two-dimensional versions (Lowell et al., 2004). In Hoover et al. (2000) a piecewise threshold is used to separate vessel pixels from non-vessel pixels in contrast to more common global threshold techniques. An alternative way to distinguish between vessels and non-vessels is supervised classification: to each pixel a feature vector is assigned containing different properties, for example grayscale, matched filter response to a wavelet filter (Soares et al., 2006), line operators (Ricci and Perfetti, 2007), directional derivatives and more (Staal et al., 2004). This method is of statistical nature and based on a training set of labels assigned by a human observer.
Multiscale analysis of images via the Gabor wavelet is done in Li et al. (2006), while the Laplacian of a Gaussian (LoG) is used by Vermeer et al. (2004) to extract vessels. Vermeer et al. derive optimal values for the standard deviation of the Gaussian and for the threshold value in order to extract bar-shaped vessels. Separable kernels composed from a second order Gaussian derivative and a window function are used by Gang et al. (2002) and M.Sofka and Stewart (2006). Gang et al. employ a box function, while Sofka and Stewart utilise a Gaussian window function. The divergence of vector fields such as the gradient field and the normalised gradient vector field is employed in Lam and Yan (2008) for the detection of vessels and vessel centrelines.
An early and efficient multiscale approach based on an orientation bundle derived from Gaussian derivatives for the detection and removal of general elongated 2D structures in images is proposed in Kalitzin et al. (1999).
The algorithms proposed in Staal et al. (2004) and Mendonça and Campilho (2006) use the centrelines as starting point for the vessel extraction. Many algorithms, such as the computation of the tortuosity of vessels (Grisan et al., 2008) can benefit from well-detected centrelines.
The detection of characteristic anatomical structures of the retina such as vascular arch, macula and optic disc is addressed in Niemeijer et al. (2007) and in Tobin et al. (2007). The investigations carried out in Youssif et al. (2008), Hoover and Goldbaum (2003) and ter Haar (2005) focus on the detection of the optic disc in particular. Finally we mention that methods from image registration are used in Stewart et al. (2003) and Matsopoulos et al. (2004) for retinal image analysis.
Quite a new approach uses vessel diameters and the angle at branching points as a quality marker for vessel segmentation (Martinez-Perez et al., 2007).

A general method for detecting general complex 3D vascular structures is devised in a recent paper of Qian et al. (2009). The proposed method is mainly applied at 3D animal vascular from both MRI and micro-CT images.

1.2 Basic assumptions

In our paper we assume that vessels are locally line-like structures. Generally, vessel profiles are modeled by a single- or a double-Gaussian, which can be derived from Bouguer's Law (Gao et al., 1997). We derive from Bouguer's Law that the cross section of the grayscale representation of a vessel has a bathtub-like shape. Hence, the second derivative of the vessel profile is above a certain positive threshold. It is not necessary at this stage to pay any attention to the middle reflex.
It is worth mentioning that in our approach the thresholding of second order derivatives leads to large connected components in vessel segmentation. We pre-smooth the vessel profile with a Gaussian before computing the second derivative. The resulting Gaussian derivative has positive sign in the interior of the vessel. An additional improvement, see Tables 2-4 of our method is achieved by performing two pre-processing steps: We regularise the original image with the edge- and coherence-enhancing anisotropic diffusion filter from Weickert (1994) followed by a morphological operation called the black-top-hat (Soille, 1999).
We saw advantages in using a localised variant of the Radon transform. This transform uses line integrals and serves as a vital ingredient in the mathematics of computerised tomography. So it is not surprising, that it has been used in Beyerer and León (2002) to enhance line-like structures in digital images.
We choose the so called *local* Radon transform, as in van Ginkel (2002), where the locality is achieved by weighting the line integrals for example by a Gaussian function. Furthermore, in contrast to the standard Radon transform, every point of interest is treated as the origin of the coordinate system. In addition to the algorithm of Vermeer et al. (2004), we analyse the second derivative integrated over a line, rather than convolving it with an isotropic Gaussian.

The structure of the paper is as follows: We introduce our vessel model in Section 2. Our main tool, the local Radon transform, is introduced in Section 3. In Section 4 the actual vessel segmentation algorithm and its computational details are explained. Section 5 is devoted to the skeletonisation algorithm and detection of the branching points. We report on experiments performed with images of the retina and the conjunctiva in section 6.

2 Vessel models

2.1 Coordinates

One of the main aspects of our vessel detection algorithm is the adaptivity to the actual vessel profile. This is achieved by convolving the image with a strongly anisotropic kernel, whose orientation is determined by a rotation angle θ.
We introduce local coordinates as shown in Fig. 1 where we depict a three-dimensional vessel model in its representation as a grayscale image. The image plane is spanned by two axes, one in direction ω and one in direction $\omega^\perp$ perpendicular to it,

$$\omega = \begin{pmatrix} \cos\theta \\ \sin\theta \end{pmatrix}, \ \omega^\perp = \begin{pmatrix} -\sin\theta \\ \cos\theta \end{pmatrix} . \tag{1}$$

The direction $\omega^\perp$ corresponds to the vessel run, while the gray-value representation of the vessel profile is represented in the ω-z plane. Later on, we will differentiate in direction ω and integrate in direction $\omega^\perp$. The grayscale intensity I at a point $p = s\omega + t\omega^\perp$ in the image plane is represented by a z-value, hence the darker inner part of the vessel attains a smaller z-value than the surrounding retina.
We assume locally constant gray values inside the vessel in the direction of $\omega^\perp$. Therefore we will treat I as a function of s only, $I = I(s)$, unless stated otherwise.

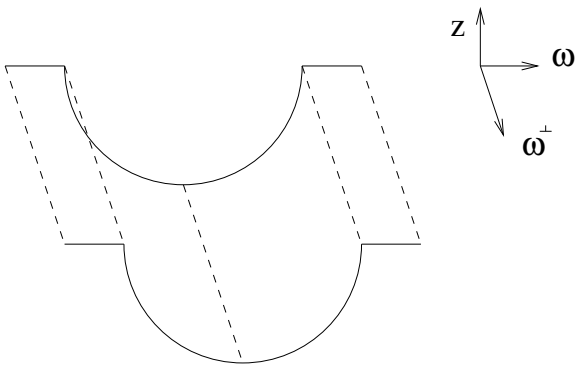

Figure 1: Vessel appearance and local coordinates, ω and $\omega^\perp$ span the image plane, z-coordinate shows the gray value

2.2 The cross section of a vessel

A simple vessel model is used by Vermeer et al. (2004) who considers a vessel as a "brightness gap" with step size h and width w.

$$I(s) = \begin{cases} c & : \quad |s| \leq w/2 \\ c+h & : \quad |s| > w/2 \end{cases} \quad . \tag{2}$$

Gao et al. (1997) and Chapman et al. (2001) use a Gaussian shaped model of a vessel. This model is derived from Bouguer's Law (Gao et al., 1997), which relates the reflected light I to the incident light I_0:

$$I(s\omega + t\omega^{\perp}) = I_0 e^{-2 \cdot \int \alpha(s,t,u)\, du} \tag{3}$$

where $\alpha(s,t,u)$ is the attenuation coefficient at the point $p = s\omega + t\omega^{\perp} + ue_3$, and u is the depth in the retina.
The idea behind formula (3) is shown in Fig. 2. The incident light I_0 passes through the vessel, and is partially absorbed. The attenuation of the light is modeled by the absorption coefficient α. It determines via equation (3) what amount of light I is received by the camera. The Gaussian shaped model

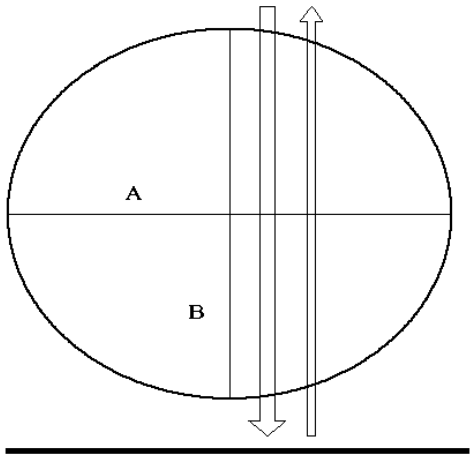

Figure 2: Light traversing through an elliptic vessel

derived from Bouguer's law in Gao et al. (1997) results from the assumption that a vessel is cylindrical with a circular cross section and that α is constant within. It states

$$I(s) = I_0 \left(1 - ae^{-\frac{s^2}{2\sigma^2}}\right), \; a, \sigma > 0 \; . \tag{4}$$

Due to the central light reflex in larger vessels, an improved model is given by a double Gaussian (Gao et al., 1997),

$$I(s) = I_0 \left(1 - ae^{-\frac{s^2}{2\sigma^2}} + be^{-\frac{s^2}{2\sigma_r^2}}\right), \tag{5}$$

with suitable $0 \leq b < a$ and $0 < \sigma_r < \sigma$.

In this article, we assume a vessel to be cylindric but now, according to anatomic reality (Naumann, 1980), with an ellipsoidal rather than a circular cross section. This is sketched in Fig. 2. Assuming α to be constant inside a vessel, we get

$$I(s) = I_0 e^{-2g(s)} , \tag{6}$$

where $g(s)$ is the length of the cross section through the elliptic vessel. According to Kak and Slaney (1988), the length $g(s)$ is given by

$$g(s) = \begin{cases} c_1 \alpha \sqrt{c_2^2 - s^2} & : \quad |s| \leq c_2 \\ 0 & : \quad |s| > c_2 \end{cases} \tag{7}$$

with appropriate constants $c_1 = 2AB/c_2^2 > 0$ and $c_2^2 = A^2 \cos^2 \psi + B^2 \sin^2 \psi > 0$ depending on the main axes A and B of the ellipse and the angle ψ between incident light and the main axis of the ellipse. Possible shapes of our vessel model I are shown in Fig. 3. For the sake of simplicity in this graphical representation we set the parameters A, B, I_0 to 1. For the attenuation coefficient α we have chosen two different values, which result in a brighter and a darker vessel appearance, for example arteries and venules.

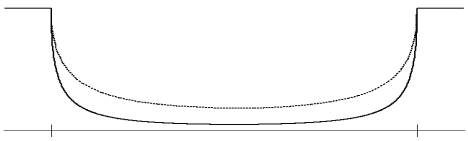

Figure 3: Our model of the intensity profile I. The dotted line indicates an artery with a small α while the continuous line corresponds to a vein with a higher α-value.

2.3 The convexity of a cross section

In the Gaussian model, the cross section of the vessel is convex in the range from $-\sigma$ to σ, since these values indicate the inflection points of a Gaussian.

In Gang et al. (2002) the vessel width is linearly related to σ, while Gao et al. (1997) specifies the vessel boundary at $r \approx 1.69\sigma$ and Chapman et al. (2001) at $r \approx 1.64\sigma$.

We derive from (6)

$$I''(s) = I(s)\left(4(g'(s))^2 - 2g''(s)\right) \ . \tag{8}$$

Since we have

$$g''(s) = -\frac{\alpha c_1 c_2^2}{(c_2^2 - s^2)^{3/2}} < 0 \tag{9}$$

inside the vessel, we obtain

$$I'' > 0 \ . \tag{10}$$

Consequently, the vessel profile of a cross section is convex. For later use, we note that (8) and (9) imply even that

$$I'' > T \tag{11}$$

for a certain strictly positive constant T. This consideration is the first building block for our vessel detection algorithm. The central light reflex is not included in our model, however, this does not mar the performance of our algorithm.

2.4 Uniform threshold despite of Gaussian smoothing

The vessel model of Vermeer et al. (2004) assumes a box-function whose boundaries coincide with the vessel boundaries. Fig. 4(a) and 4(b) show the cross sections of the box model of Vermeer (left column)) and our novel light attenuation model (right column). The Gaussian derivatives are displayed in the subsequent pictures shown in Fig. 4(c)-4(f). Our model has an important advantage over the one of Vermeer et al. model. Vermeer et al. determines the interior of the vessel via a carefully chosen threshold depending on the relation of the Gaussian standard deviation σ and the vessel width. For small σ the Gaussian derivative will be close to zero in the middle section of the vessel making it very difficult to find a suitable threshold that determines the interior of the vessel correctly.
Numerical considerations show that the Gaussian derivative of our profile function does not approach zero at any interior point of the vessel, no matter how large or, more important, how small σ is, see Fig. 4(d) and Fig. 4(f). Hence our model allows for a uniform threshold that can be chosen independently of the Gaussian smoothing parameter σ. This behaviour can

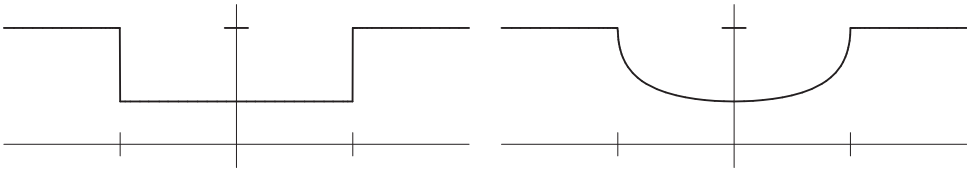

(a) Model of Vermeer et al. (b) Our model

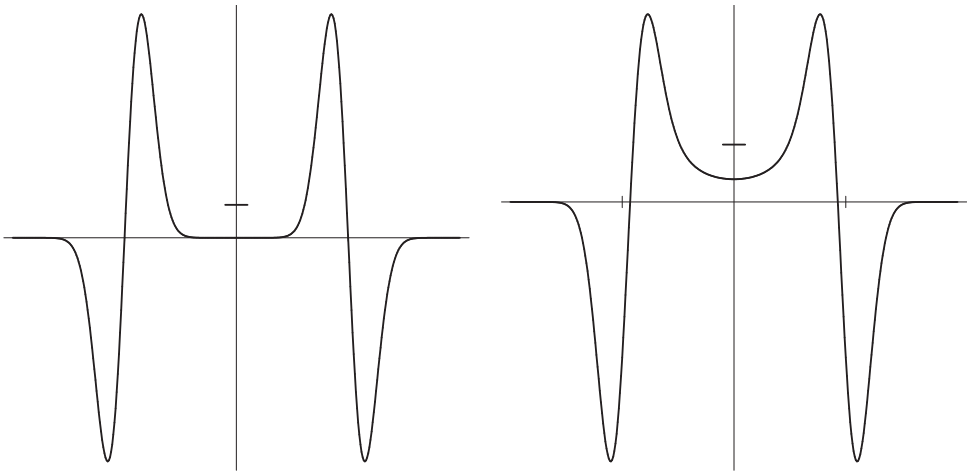

(c) Model of Vermeer et al., $\sigma = 0.15$ (d) Our model, $\sigma = 0.15$

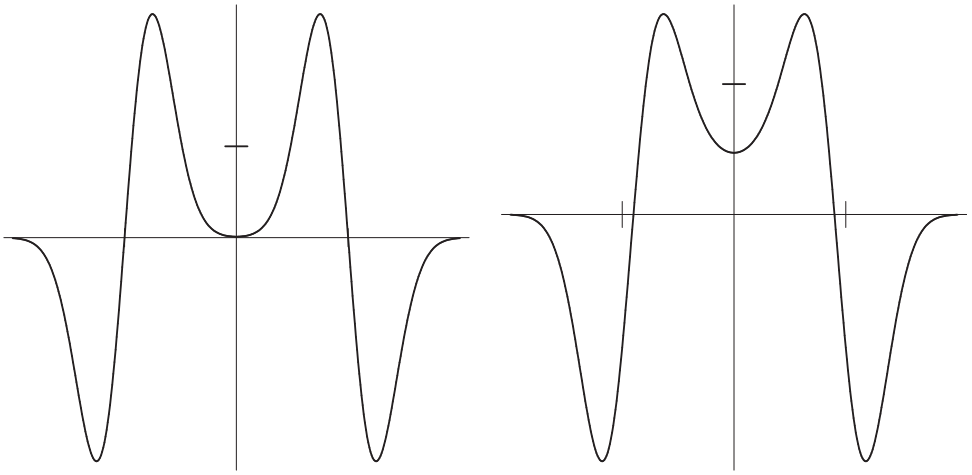

(e) Model of Vermeer et al., $\sigma = 0.25$ (f) Our model, $\sigma = 0.25$

Figure 4: Comparison: Model of Vermeer et al. vs. our model. First row: vessel models. Middle row: second order Gaussian derivative with $\sigma = 0.15$. Last row: the same with $\sigma = 0.25$. For presentational reasons the images are scaled individually in height. The marks on the axes indicate unit length.

be attributed to the strict convexity of our profile function in the interior of the vessel. Note that this independence does not refer to the parameters of the vessel, $\alpha, c_1, c_2,\ I_0$. Nevertheless choosing a proper threshold is still an issue, since there is undeniably a dependency on illumination artefacts, for example. However, the dependency on the noise level poses no severe problem since by design of our algorithm (local Radon transform) the vessel tree is recognised as a large connected component allowing for a quite liberal choice of a threshold value. The connected components associated with noise and induced by a potentially too small threshold are in general very small and hence easily eliminated by our method, for more details see section 4.5.

3 The local Radon transform

In the last sections we have developed a vessel model that assumes a convex vessel cross section. However, real data suffer from noise or other disturbances and hence might not fulfil this model assumption. Therefore the real image has to be processed with a transform that both regularises the data and preserves or even enhances convexity of blood vessel cross sections.
To this end it is advantageous to introduce a new polar coordinate system that is used in a similar form in computerised tomography. We consider I as a function of s, t in a point $p = x + s\omega + t\omega^{\perp}$ for a fixed x. The regularising effect is achieved by averaging with a Gaussian K_ρ in the direction $\omega^{\perp}$ of the vessel. However, we cannot predict the vessel run, and choosing a Gaussian as a weight function takes this uncertainty into account. This leads us to the local Radon transform of I van Ginkel (2002):

$$R_L I(x, \omega, s) = \int_{-\infty}^{\infty} K_\rho(t) I(x + s\omega + t\omega^{\perp})\, dt. \tag{12}$$

As an integral transform R_L produces indeed a regularised version of I. Remarkably, the convexity of the cross sections carries over to its Radon transform:

$$\begin{aligned} (R_L I)''(x, \omega, s) &:= \int_{-\infty}^{+\infty} K_\rho(t) \frac{\partial^2}{\partial s^2} I(x + s\omega + t\omega^{\perp}) dt \\ &\geq T \int_{-\infty}^{+\infty} K_\rho(t)\, dt = T\ , \end{aligned} \tag{13}$$

where we have used the assumption $\frac{\partial^2}{\partial s^2} I(x + s\omega + t\omega^{\perp}) > T$ and that $\int_{-\infty}^{+\infty} K_\rho(t)\, dt = 1$. In Krause (2006) the local Radon transform has been used to detect edges in digital images.

4 Retinal Vessel Segmentation

4.1 Criterion for vessel segmentation

In order to use the local Radon transform and its derivative to decide whether a point x is a vessel point or not, we consider $(R_L f)''(x, \omega, 0)$ as a function of ω alone for a fixed point x,

$$\omega \mapsto (R_L I)''(x, \omega, 0) \ . \tag{14}$$

We select an optimal direction ω_x according to the following strategy: ω_x is the direction that maximises $(R_L I)''(x, \omega, 0)$.
Then we recognise x as a vessel point if

$$(R_L I)''(x, \omega_x, 0) > T \ . \tag{15}$$

It is important to remark that for the classification of the vessel points the accurate estimation of the vessel direction is not crucial due to the employed threshold technique (15).

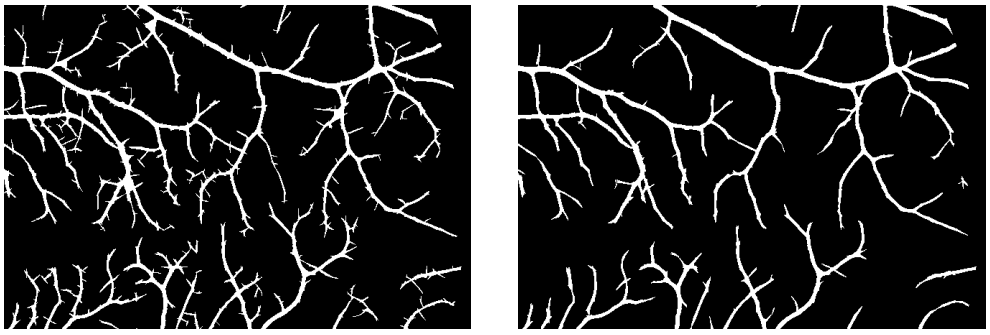

(a) Segmentation without anisotropic diffusion

(b) Segmentation on anisotropic diffusion filtered image

Figure 5: Effects of anisotropic diffusion

4.2 Details of computation

We compute the second derivative via a central difference with step size $h = 1$, as we assume the image to be sampled with that grid size. The resulting approximation $H(x, \omega)$ to $(R_L I)''(x, \omega, 0)$ is given by

$$\begin{aligned} H(x, \omega) = \ & R_L I(x, \omega, -1) \\ & -2R_L I(x, \omega, 0) \\ & +R_L I(x, \omega, 1) \ . \end{aligned} \tag{16}$$

In our basic assumptions vessels are always convex. Hence points with $H(x,\omega) < 0$ for all ω are of no interest. Therefore we can restrict our attention to the function

$$\mathrm{res}(x) = \max(0, \max_{\omega} H(x,\omega)) \ . \tag{17}$$

Vessel points x are characterised by $\mathrm{res}(x) > T$.

4.3 Techniques for Preprocessing

In the preprocessing steps we use a well established smoothing technique called edge- and coherence-enhancing anisotropic diffusion (ECED) (Weickert, 1994). It produces simplified versions $u(x,t)$ of the original image $I(x)$ as solutions of the nonlinear partial differential equation

$$\partial_t u = \mathrm{div}\,(D(u)\nabla_x u) \tag{18}$$

$$u(\cdot,0) = I \tag{19}$$

subjected to Neumann boundary conditions. Here D denotes a symmetric positive definite matrix (diffusion tensor) that adaptively encodes dominant directional information in the evolving image u and steers the evolution process governed by (18). For further details the reader is referred to Weickert (1994). Furthermore, in early experiments it became apparent that the brightness of the optic disc was responsible for erroneous results at its boundary. These errors can be diminished by using a classical morphological operator, namely the black top hat, followed by an image inversion. Detailed information about morphological operators are provided, for example, in Soille (1999).

4.4 Efficient implementation

We can implement the calculation of H as convolutions with pre-computed kernels g_ω, in the ω-$\omega^\perp$-coordinate system exploiting the symmetry of both the Radon kernel and the Gaussian kernel. To see this we assume x to be 0, and we approximate $R_L I(0,\omega,l)$ with a trapezoid rule,

$$R_L I(0,\omega,l) \approx \sum_{k\in\mathbb{Z}} K_\rho(k) I(l\omega + k\omega^\perp) \ . \tag{20}$$

The points where I has to be evaluated are approximated by bilinear interpolation which leads to a formula of the form

$$R_L I(0, \omega, l) \approx \sum_{m \in \mathbb{Z}^2} \alpha_m I(m) \tag{21}$$

with weights $\alpha_m = \alpha_m(\omega)$. From the central difference quotient in (16) we obtain

$$H(0, \omega) \approx \sum_{m \in \mathbb{Z}^2} g_\omega(m) I(m) \tag{22}$$

for some g_ω. The approximation of $H(x, \omega)$ at an arbitrary point x can be obtained by a convolution with the symmetric kernels g_ω,

$$H(x, \omega) = (I * g_\omega)(x) \ . \tag{23}$$

Since g_ω have a small support the convolutions with the pre-computed kernels g_ω are highly efficient.

4.5 Eliminating small connected components

To counteract the fact that our algorithm might produce false positives in addition to real vessels, see Fig. 7(c), we have to ensure that only relevant components are recognised as vessels. Small connected components are dismissed as non-vessels. The components and their size are computed via a Union-Find algorithm (Cormen et al., 1990).
The central light reflex establishes a relatively small non-vessel component which is completely surrounded by an already detected vessel. As before these small components are identified with the help of a Union-Find algorithm and then turned into vessel points.

5 Skeletonisation

5.1 Skeletonisation algorithm

In order to obtain a more abstract representation of the vessels we construct a graph-like structure, the so called 1-pixel wide vascular tree (Chanwimaluang and Fan, 2003). This representation facilitates the analysis of the vessel. To this end we apply a skeletonisation algorithm as described, for example, in Gonzalez and Woods (2002). The employed procedure is a prairie-fire algorithm, avoiding the well-known failures of other thinning-line algorithms (Wang et al., 2007). As a result of the algorithm connectivity patterns of the vessel structure are represented correctly by the obtained skeleton.

5.2 Detection of branching points

The first step in the analysis of the skeleton is to determine its branching points. For this purpose we employ the following procedure inspired by the above skeletonisation algorithm. We consider a 5×5 square with centre point p_1 as indicated in Fig. 6. Next we generate a finite sequence $v_2, v_3, \ldots, v_{17}, v_2$ with

$$v_i = \begin{cases} 1 & \text{if } p_i \text{ is a skeleton point} \\ 0 & \text{else} \end{cases} \tag{24}$$

Now we associate to the center pixel p_1 a value $N(p_1)$ as the number of

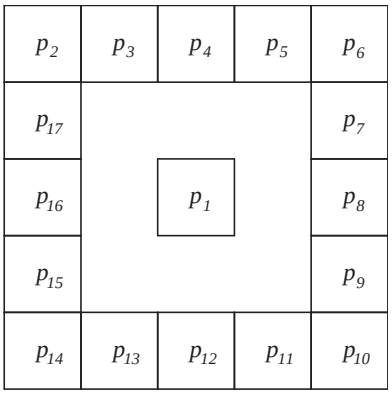

Figure 6: The center point p_1 and a 5×5-square

0-1-transitions in the sequence $\{v_i\}_{i=2,3,\ldots,17,2}$. The point p_1 is marked as branching point if $N(p_1) \geq 3$. However, with this method several points may qualify as branching points for the same furcation. In order to single out a unique branching point for each furcation the procedure described above is repeated with a smaller 3×3-square. Note that endpoints p of the skeleton are characterised by $N(p) = 1$.

6 Experiments

Our algorithm works on scalar images, so we converted colour images (RGB 8 bit) into grayscale images by using convert from the package ImageMagick from imagemagick.org (2008) in order to incorporate information from all channels, that is $0.299 \cdot R + 0.587 \cdot G + 0.114 \cdot B$.

6.1 Preprocessing

In order to improve our results, mainly to eliminate false positives, we first perform some preprocessing steps before applying our model algorithm to the images.

1. Performing only four timesteps of an explicit discretisation of the anisotropic diffusion equation (18) entails a slight improvement of our results by avoiding the creation of false positives at the vessel boundaries, see Tables 2-4 and image 5. A more excessive use of this smoothing technique would lead to a deterioration of the final results.

2. In all the images of the considered database the field of view (FOV) is surrounded by dark background pixels. In order to avoid undesired boundary effects, we either cut out the FOV (STARE database) or extend the FOV by a circular mirroring and inpainting-type process (DRIVE database).

3. An inverted black top hat as mentioned in section 4.3 diminishes the rate of false positive classifications caused by the optic disc.

6.2 Results on our clinical database

Fig. 7 shows the results of our segmentation results of our clinical database, where the images have been created by a Topcon NW200 camera (resolution 2048×1536)). This database consists of nearly 11.000 patients and about 37.000 images.
Pre-smoothing via anisotropic diffusion and the application of the local Radon transform results in Fig. 7(b). Further thresholding, Fig. 7(c), and subsequent automatic removal of smaller disturbances and false positives, according to the procedure described in subsection 4.5, leads to Fig. 7(d).
For better visualisation of the final skeletonised result Fig. 8(b) we zoom into the marked section in Fig. 7(a). A comparison of the images Fig. 8(a) and Fig. 8(b) confirms that the vessel structure is adequately and correctly represented by the skeleton.

6.3 Evaluation on DRIVE- and STARE-Database

When applying our method the the STARE- and DRIVE database we follow the standard rules described in detail in Mendonça and Campilho (2006), Staal et al. (2004) and Hoover et al. (2000). Table 1 shows the parameter settings of our experiments. The noise scale σ refers to the standard deviation of the Gaussian pre-smoothing that was performed for regularisation.

The integration scale ρ determines the size of the applied local Radon kernel. The numbers in the last line in Table 1 indicate the minimal size (in terms of numbers of pixels) of the connected components that are displayed in the final result. Connected components that have less pixels than the user defined number have been eliminated. The specific results of our experiments are displayed in Tables 2-4. For comparison and examples, see Fig. 9 and 10. The computing time of our algorithm for an image of the DRIVE database is about 18 seconds including anisotropic diffusion filtering, mirroring and black-top-hat, and about the same time for the STARE database performed on a Dual-core Pentium PC (1.86 Ghz, 2 GB RAM). Note that the running time for segmentation may be more important in the future as our actual resolution (own database) has an approximately 18 times, the estimated future standard even 64 times more amount of data compared to the DRIVE- and STARE-database images. We performed our own implementation in C++ (using g++ on Linux).
The bold letters indicate the best results in the following categories:

$$\text{accuracy} = \frac{\text{number of correctly classified pixels}}{\text{total number of pixels}},$$

$$\text{true positives} = \frac{\text{number of detected vessel pixels}}{\text{total number of true vessel pixels}},$$

$$\text{and false positives} = \frac{\text{number of falsely detected vessel pixels}}{\text{total number of non-vessel pixels}}.$$

For both databases, our method leads to the smallest rate of false positives among all techniques. Concerning the STARE-database, the method of Staal seems to be better than our method. Nevertheless, with respect to accuracy our methods outperforms the other approaches.

Table 1: PARAMETER SETTINGS USED FOR VESSEL SEGMENTATION

Parameter	DRIVE images	STARE images	our clinical database
σ	1.75	1.75	2
ρ	4.5	4.5	6
size of connected comp.	25	25	100

6.4 Comparison with other second order filters

Our method belongs to the class of matched filter approaches. This class includes the concepts presented by Gang et al. (2002) and M.Sofka and Stewart (2006) as well. Both groups use separable kernels. Gang et al. calculate

Table 2: PERFORMANCE OF VESSEL SEGMENTATION METHODS (DRIVE IMAGES)

Method	Accuracy	True positive	False positive
Human observer, (Niemeijer and van Ginneken, 2002)	**0.9473**	**0.7761**	0.0275
Our method (without anisotr. diff.)	0.9439	0.6831	0.0183
Our method (with anisotr. diff.)	0.9442	0.6848	0.**0182**
Mendonça (gray-intensity)	0.9463	0.7315	0.0219
Mendonça (green-channel)	0.9452	0.7344	0.0236
Staal (Staal et al., 2004), (Niemeijer and van Ginneken, 2002)	0.9442	0.7194	0.0227
Niemeiijer (Niemeijer et al., 2004), (Niemeijer and van Ginneken, 2002)	0.9417	0.6898	0.0304

Table 3: PERFORMANCE OF VESSEL SEGMENTATION METHODS (STARE IMAGES; WITH FOV)

Method	Accuracy	True positive	False positive
Human observer, (Niemeijer and van Ginneken, 2002)	0.9354	**0.8949**	0.0610
Our method (without anisotr. diff.)	0.9482	0.6518	**0.0171**
Our method (with anisotr. diff.)	0.9485	0.6632	0.0182
Mendonça (a^* component)	0.9479	0.7123	0.0242
Mendonça (luminance)	0.9421	0.6764	0.0266
Mendonça (green)	0.9440	0.6996	0.0270
Staal, (Niemeijer and van Ginneken, 2002)	**0.9516**	0.697	0.019
Hoover (Hoover et al., 2000), (Hoover, 2000)	0.9267	0.6751	0.0433

Table 4: PERFORMANCE OF VESSEL SEGMENTATION METHODS (STARE IMAGES-NORMAL VERSUS ABNORMAL CASE)

Method	Accuracy	True positive	False positive
	Normal cases		
Human observer, (Niemeijer and van Ginneken, 2002)	0.9283	**0.9646**	0.0764
Our method (without anisotr. diff.)	**0.9537**	0.7104	**0.0164**
Our method (with anisotr. diff.)	0.9536	0.7169	0.0174
Mendonça (a^* component)	0.9531	0.7366	0.0178
Mendonça (luminance)	0.9477	0.7109	0.0206
Mendonça (green)	0.9492	0.7258	0.0209
Hoover, (Hoover et al., 2000), (Hoover, 2000)	0.9324	0.6766	0.0338
	Abnormal cases		
Human observer, (Niemeijer and van Ginneken, 2002)	0.9425	**0.8252**	0.0456
Our method (without anisotr. diff.)	0.9430	0.5964	**0.0177**
Our method (with anisotr. diff.)	**0.9437**	0.6046	0.0179
Mendonça (a^* component)	0.9426	0.6801	0.0306
Mendonça (luminance)	0.9364	0.6420	0.0326
Mendonça (green)	0.9388	0.6733	0.0331
Hoover, (Hoover et al., 2000), (Hoover, 2000)	0.9211	0.6736	0.0528

a Gaussian derivative perpendicular to the vessel direction multiplied with a box function in tangential direction. Instead, Sofka and Stewart use a Gaussian convolution in tangential direction as well. However, our matched filter computes finite difference approximations of the second order derivative combined with true Gaussian weighted line integrals that are obtained by interpolation. This enhances the localisation of our kernel and lowers the computational load in comparison with Sofka and Stewart and Gang et al. In order to show the ability of our algorithm to close gaps in interrupted lines we compare it to a second order differential filter, the Haralick operator (HO) (Haralick, 1984). which computes the second order derivative in gradient direction. The result of the classical HO when applied to the original image is depicted in Fig. 11(b). In comparison with the result of our local Radon transform as displayed in Fig. 11(a) it becomes apparent that th HO operator produces a less smooth result with fluctuating vessel intensities that even lead to pseudo-interruptions of the vessels. Both in the case of local Radon transform and HO operator negative values are mapped to zero. Fig. 11(a) brings to light an important feature of the local Radon transform, namely its capability to close gaps in line-like structures.

6.5 Conjunctiva vessels

Our detection algorithm does not depend on the presence of a typical geometric pattern or other a-priori information about the vessel-tree structure. This is confirmed by the results obtained from applying our detection algorithm on two images of conjunctiva vessels, Fig. 12(a) and Fig. 12(b). Despite the poor image quality, the characteristic vessel structure is found without pre-processing or parameter tuning, see Fig.12(c) and Fig. 12(d).

7 Conclusion

This paper starts with the assumption of an ellipsoidal cross-section of real world vessels. Using the light-attenuation model expressed by Bouguer's law we derive a vessel intensity model that employs convexity properties of the describing functions. We use the local Radon transform to process vessel images for three reasons: first it has a regularising effect on the image, second it detects and enhances line-like structures, and important, it preserves convexity properties of our intensity model which are captured by second order derivatives. The performance of the local Radon transform can be improved by a preprocessing via an anisotropic diffusion filter. The obtained results allow the application of a skeletonisation algorithm leading to an accurate

representation of the vessel-tree and its ramification. The proposed method is conceptionally simple, robust and universally applicable as the example of the conjunctiva vessel detection may demonstrate. In the future we intend to extend our algorithm to be part of a learning system.

Acknowledgement

We thank the authors of the DRIVE and STARE database for making their database available and thus allowing us to evaluate our results. Furthermore we like to thank Rüdiger Leilich, Software Engineer, for providing us the tool "Algo-Verifier" for better visualisation and documentation the very detailed image information and documentation of results, experiments and proceedings in a specifically designed database.

References

Beyerer, J., León, F. P., 2002. Die Radontransformation in der digitalen Bildverarbeitung. Automatisierungstechnik 50, 472–480.

Chanwimaluang, T., Fan, G., 2003. An efficient algorithm for extraction of anatomical structures in retinal images. In: Proc. IEEE International Conference on Image Processing. pp. 1093–1096.

Chapman, N., Witt, N., Bharat, A., et al., 2001. Computer algorithms for the automated measurement of retinal arteriolar diameters. British Journal of Ophtalmology 85, 74–79.

Cormen, T. H., Leiserson, C. E., Rivest, R. L., 1990. Introduction to algorithms. MIT Press.

Cree, M. J., Cornforth, D., Jelinek, H. F., 2005. Vessel segmentation and tracking using a two-dimensional model. In: Proceedings of the Image and Vision Computing Conference. University of Otago, New Zealand, pp. 345–350.

Gang, L., Chutape, O., Krishnan, M., 2002. Detection and measurement of vessels in fundus images using amplitude modified second-order Gaussian filter. IEEE Transactions on Biomedical Engineering 49 (2), 168–172.

Gao, X., Bharat, A., Hughes, A., et al., 1997. Towards retinal vessel parameterization. In: Medical Imaging 1997: Image Processing. Vol. 3034. SPIE Proc., pp. 734–744.

Gonzalez, R., Woods, R., 2002. Digital Image Processing. Prentice Hall, New Jersey.

Grisan, E., Foracchia, M., Ruggeri, A., 2008. A novel method for the automatic grading of retinal vessel tortuosity. IEEE Transactions on Medical Imaging 27 (3), 310–319.

Haralick, R., 1984. Digital step edges from zero crossing of second directional derivatives. IEEE Transactions on Pattern Analysis and Machine Intelligence 6 (1), 58–68.

Hoover, A., 2000. Stare database.
URL `http://www.ces.clemson.edu/~ahoover/stare`

Hoover, A., Goldbaum, M., 2003. Locating the optic nerve in a retinal image using the fuzzy convergence of the blood vessels. IEEE Transactions on Medical Imaging 22 (8), 951–958.

Hoover, A., Kouznetsova, V., Goldbaum, M., 2000. Locating blood vessels in retinal images by piecewise threshold probing of a matched filter response. IEEE Transactions on Medical Imaging 19 (3), 203–210.

imagemagick.org, 2008. Imagemagick.
URL `http://www.imagemagick.org`

Jelinek, H., Depardieu, C., Lucas, C., Cornforth, D., Huang, W., Cree, M., 2005. Towards vessel characterisation in the vicinity of the optic disc in digital retinal images. In: Proceedings of the Image and Vision Computing Conference. University of Otago, New Zealand.

Kak, A., Slaney, M., 1988. Principles of Computerized Tomographic Imaging. IEEE Press, New York.

Kalitzin, S., Ter Haar Romeny, B., Viergever, M., 1999. Invertible apertured orientation filters in image analysis. International Journal of Computer Vision 31, 145–158.

Krause, M., 2006. Corner detection in digital images using local tomography. Bachelor's thesis, Dept. of Mathematics and Computer Science, Saarland University.

Lam, B., Yan, H., 2008. A novel segmentation algorithm for pathological retina images based on the divergence of vector fields. IEEE Transactions on Medical Imaging 27 (2), 237–246.

Li, Q., You, J., Zhang, L., Bhattacharya, P., 2006. Automated retinal vessel segmentatin using Gabor filters and scale multiplication. In: SMC '06 IEEE International Conference on Systems, Man and Cybernetics. Vol. 4. pp. 3521–3527.

Lowell, J., Hunter, A., Steel, D., Basu, A., Kennedy, R. L., 2004. Measurement of retinal vessel widths from fundus images based on 2-D modeling. IEEE Transactions on Medical Imaging 23 (10), 1196–1204.

Martinez-Perez, M. E., Hughes, A. D., Thom, S. A., Bharath, A. A., Parker, K. H., 2007. Segmentation of Blood Vessels from Red-free and Fluorescein Retinal Images. Medical Image Analysis 11 (1), 47–61.

Matsopoulos, G., Asvestas, P., Mouravliansky, N., Delibasis, K., 2004. Multimodal registration of retinal images using self organizing maps. IEEE Transactions on Medical Imaging 23 (12), 1557–1563.

Mendonça, A. M., Campilho, A., 2006. Segmentation of retinal blood vessels by combining the detection of centerlines and morphological reconstruction. IEEE Transactions on Medical Imaging 25 (9), 1200–1213.

M.Sofka, Stewart, C., 2006. Retinal vessel centerline extraction using multiscale matched filters, confidence and edge measures. IEEE Transactions on Medical Imaging 25 (12), 1531–1546.

Natterer, F., 1986. The Mathematics of Computerized Tomography. Teubner, Wiley.

Naumann, G. O. H., 1980. Pathologie des Auges II. Springer, p. 583.

Niemeijer, M., Abràmoff, M., van Ginneken, B., 2007. Segmentation of the optic disc, macula and vascular arch in fundus photographs. IEEE Transactions on Medical Imaging 26 (1), 116–127.

Niemeijer, M., Staal, J., van Ginneken, B., Loog, M., Abrámoff, M., 2004. Comparative study of retinal vessel segmentation methods on a new publicly available database. In: Proc. SPIE Medical Imaging. Vol. 5370. M. Fitzpatrick and M. Sonka, Eds., pp. 648–656.

Niemeijer, M., van Ginneken, B., 2002. Drive database.
URL `http://www.isi.uu.nl/Research/Databases/DRIVE/results.php`

Qian, X., Brennan, M. P., Dione, D. P., Dobrucki, L. W., Jackowski, M. P., Breuer, C. K., Sinusas, A. J., Papademetris, X., 2009. A nonparametric

vessel detection method for complex vascular structures. Medical Image Analysis 13, 49–61.

Ricci, E., Perfetti, R., 2007. Retinal blood vessel segmentation using line operators and support vector classification. IEEE Transactions on Medical Imaging 26 (10), 1357–1365.

Rieder, A., Dietz, R., Schuster, T., 2000. Approximate inverse meets local tomography. Mathematical Methods in the Applied Sciences 23, 1373–1387.

Soares, J. V. B., Leandro, J. J. G., Cesar, Jr., R. M., Jelinek, H. F., Cree, M. J., 2006. Retinal vessel segmentation using the 2-D Gabor wavelet and supervised classification. IEEE Transactions on Medical Imaging 25 (9), 1214–1222.

Soille, P., 1999. Morphological Image Analysis. Springer.

Staal, J., Abrámoff, M. D., Viergever, M. A., van Ginneken, B., 2004. Ridge-based vessel segmentation in color images of the retina. IEEE Transactions on Medical Imaging 23 (4), 501–509.

Stewart, C., Tsai, C.-L., Roysam, B., 2003. The dual-bootstrap iterative closest point algorithm with application to retinal image registration. IEEE Transactions on Medical Imaging 22 (11), 1379–1394.

ter Haar, F., 2005. Automatic localization of the optic disc in digital colour images of the human retina. M. Sc. thesis, Utrecht University, Utrecht, The Netherlands.

Tobin, K., Chaum, E., Govindasamy, P., Karnowski, T., 2007. Detection of anatomic structures in human retinal imagery. IEEE Transactions on Medical Imaging 26 (12), 1729–1739.

van Ginkel, M., 2002. Image analysis using orientation space based on steerable filters. Ph.D. thesis, Delft University of Technology.
URL `http://www.ph.tn.tudelft.nl/~michael/publications.html`

Vermeer, K., Vos, F., Lemij, H., Vossepoel, A., 2004. A model based method for retinal blood vessel detection. Computers in Biology and Medecine 34, 209–219.

Wang, L., Bhalerao, A., Wilson, R., 2007. Analysis of retinal vasculature using a multiresolution Hermite model. IEEE Transactions on Medical Imaging 26 (2), 137–152.

Weickert, J., 1994. Scale-space properties of nonlinear diffusion filtering with a diffusion tensor. Technical report No. 110, Laboratory of Technomathematics, University of Kaiserslautern, Germany.

Youssif, A. A.-H. A.-R., Ghalwash, A., Sabry, A.-R., Ghoneim, A.-R., 2008. Optic disc detection from normalized digital fundus images by means of a vessels' direction matched filter. IEEE Transactions on Medical Imaging 27 (1), 11–18.

(a) Original image

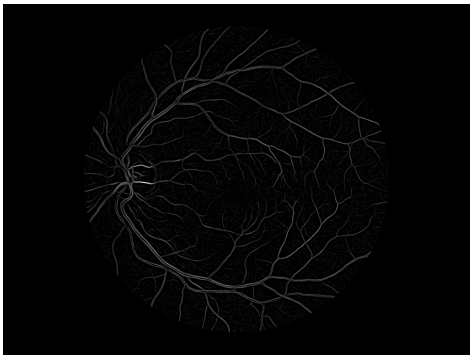

(b) Application of the local Radon transform

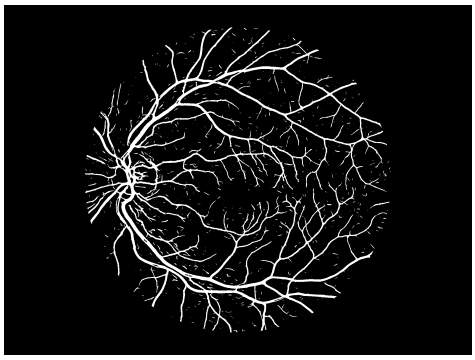

(c) Thresholded image

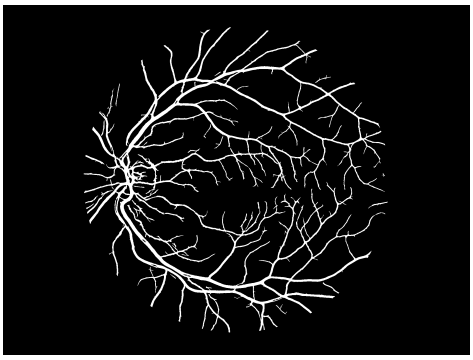

(d) Show only larger connected components

Figure 7: Results of our algorithm - own clinical database

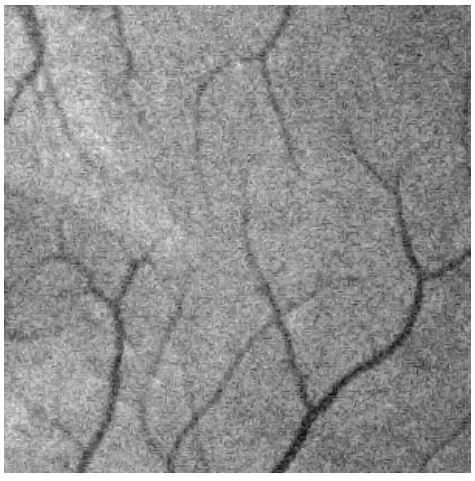

(a) Subimage of the original image, rescaled for better visualisation

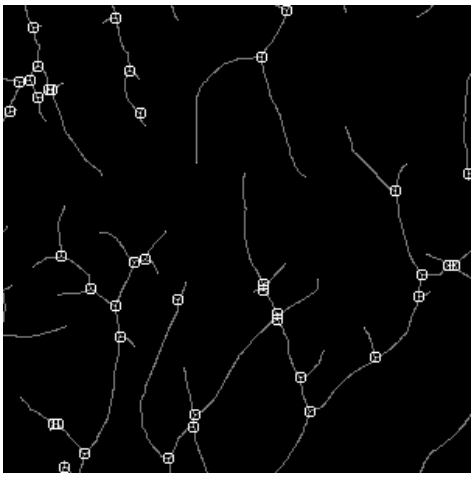

(b) Skeleton with branching points

Figure 8: Results of the skeletonisation algorithm - own clinical database

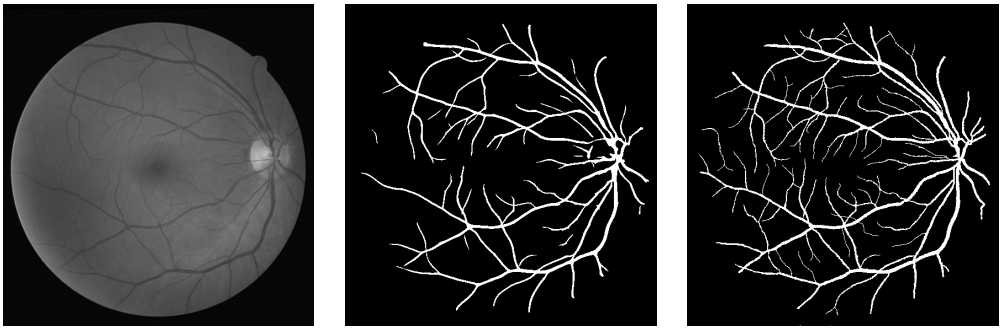

(a) Original (b) Segmentation (c) Ground truth

Figure 9: Results of our algorithm on DRIVE-database

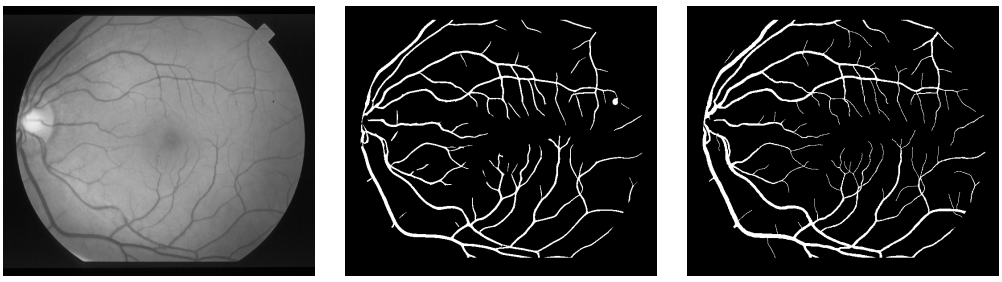

(a) Original, normal case (b) Segmentation, cropped at boundary (c) Ground truth, cropped at boundary

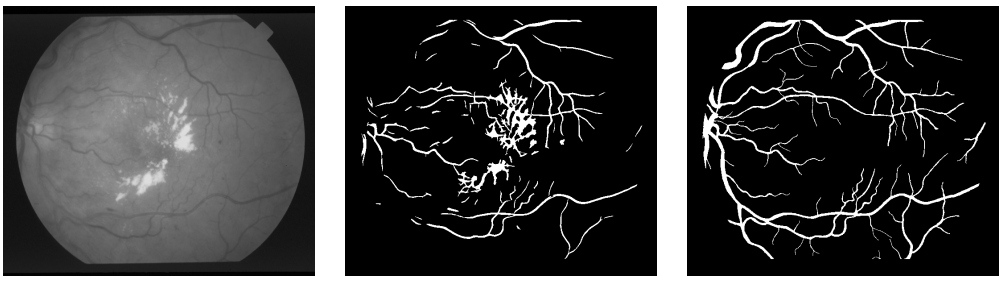

(d) Original, abnormal case (e) Segmentation, cropped at boundary (f) Ground truth, cropped at boundary

Figure 10: Results of our algorithm on STARE-database,

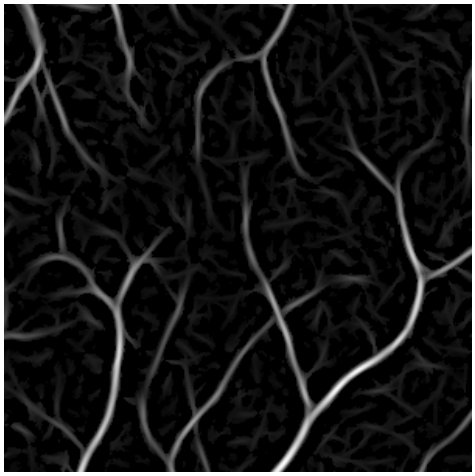

(a) Local Radon transform

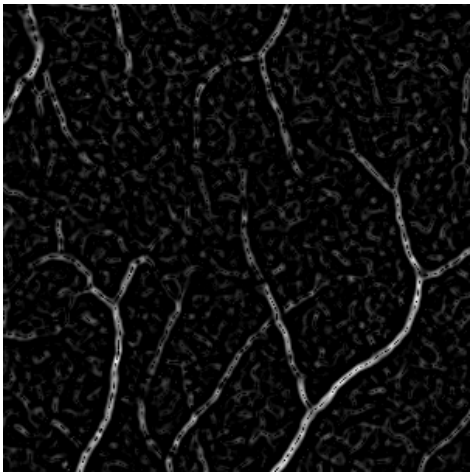

(b) Haralick operator, noise scale $\sigma = 2.0$

Figure 11: Comparison with Haralick operator, no anisotropic diffusion on input image

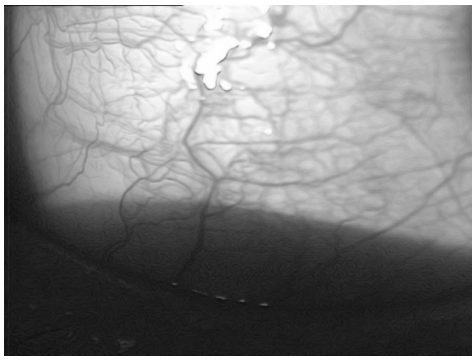

(a) Original image 1

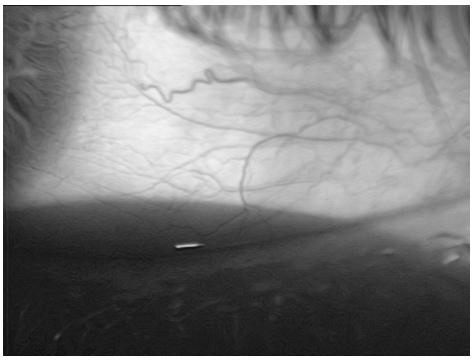

(b) Original image 2

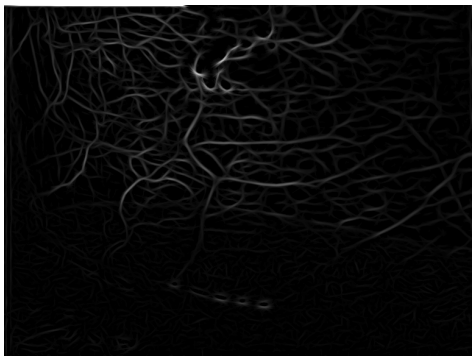

(c) Intermediate result of input image 1, brightened for visualisation

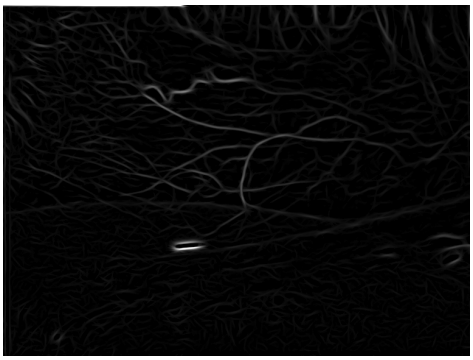

(d) Intermediate result of input image 2, brightened for visualisation

Figure 12: Human conjunctiva